

Constraint preserving boundary conditions for the Baumgarte-Shapiro-Shibata-Nakamura formulation in spherical symmetry

Miguel Alcubierre^{1,*} and Jose M. Torres^{1,†}

¹*Instituto de Ciencias Nucleares, Universidad Nacional Autónoma de México, A.P. 70-543, México D.F. 04510, México.*

(Dated: November 7, 2014)

We introduce a set of constraint preserving boundary conditions for the Baumgarte-Shapiro-Shibata-Nakamura (BSSN) formulation of the Einstein evolution equations in spherical symmetry, based on its hyperbolic structure. While the outgoing eigenfields are left to propagate freely off the numerical grid, boundary conditions are set to enforce that the incoming eigenfields don't introduce spurious reflections and, more importantly, that there are no fields introduced at the boundary that violate the constraint equations. In order to do this we adopt two different approaches to set boundary conditions for the extrinsic curvature, by expressing either the radial or the time derivative of its associated ingoing eigenfield in terms of the constraints. We find that these boundary conditions are very robust in practice, allowing us to perform long lasting evolutions that remain accurate and stable, and that converge to a solution that satisfies the constraints all the way to the boundary.

PACS numbers: 04.20.Ex, 04.25.D-, 02.30.Jr

I. INTRODUCTION

The numerical studies of solutions of the field equations of General Relativity greatly improved once the different research groups turned to modified formulations of the Arnowitt-Deser-Misner (ADM) evolution equations [1] in order to have a well-posed strongly hyperbolic system. Empirically it has been found that the Baumgarte-Shapiro-Shibata-Nakamura (BSSN) formulation [2, 3] is very robust in practice, and during the last decade it has been employed in many studies of black hole collisions, dynamics of compact objects, and its associated gravitational radiation. The BSSN formulation has two major differences when compared to the standard ADM evolution equations: the first one is a conformal decomposition of the metric and extrinsic curvature in order to isolate the volume element and the trace of the extrinsic curvature and treat them as independent variables; the second one is the promotion of the *connection functions* $\Gamma^i := \gamma^{mn}\Gamma_{mn}^i$ to independent variables, plus the fact that their resulting evolution equations are then modified by adding multiples of the momentum constraints (which vanish for physical solutions) in order to improve stability. The robustness of the formulation can be traced to this last step since it can be shown that it renders the system strongly hyperbolic.

It has been established since Friedrichs pioneering work on the structure of the initial value problem (IVP) for different reductions of the Einstein field equations, that the hyperbolicity properties play a crucial role for the robustness of the resulting evolution systems (see [4–6], and for recent reviews [7, 8]). A general result for hyperbolic systems of partial differential equations (PDE's) is that

strong hyperbolicity implies well-posedness. An important fact that has to be stressed is that this result assumes that the functions that define the system are defined on an unbounded domain. On the other hand, practical uses of an IVP scheme require the inclusion of artificial boundaries, and the way we handle the boundary conditions may spoil the well-posedness of a strongly hyperbolic system. For this reason many researchers have studied the formulation of General Relativity as an initial-boundary value problem (IBVP) [9–19]. As a result of these studies it has been demonstrated that for many formulations, and corresponding boundary conditions, the IBVP is in fact well-posed. In particular, recent advances towards this end have been achieved for the case of the Z4 system [20, 21], but very little has been done for the case of the BSSN formulation [22].

A separate issue that arises from the boundary conditions applied at artificial boundaries in the case of General relativity is the fact that they may generally not be adapted to the constraint equations in the sense that, even if the IBVP is well-posed, there are violations of the constraints introduced at the boundary that can propagate inward throughout the whole computational domain. This issue has also been considered carefully by studying the propagation of the different fields at the boundary [23–29]. However, up to this date it is not yet clear how to construct general constraint preserving boundary conditions adapted to the BSSN evolution system that can be easily implemented in a numerical evolution code.

In this work we analyze the special case of BSSN in spherical symmetry [30, 31], and based on its hyperbolic structure we obtain a set of boundary conditions that preserve the constraints, are very simple to implement, and allow one to perform long-lasting, robust and convergent simulations. At the moment our discussion is restricted to the case of asymptotically flat spacetimes. Cosmological spacetimes require a somewhat different treatment,

*Electronic address: malcubi@nucleares.unam.mx

†Electronic address: jose.torres@nucleares.unam.mx

particularly in the gauge and matter sectors, and we will consider that case in a future work.

This paper is organized as follows: We first introduce in Section II the BSSN formulation in spherical symmetry as presented in [31], then in Section III we study the characteristic structure of the evolution system in order to identify the incoming and outgoing modes. After that, in Sections IV, V and VI we make use of the incoming modes to apply consistent boundary conditions, and focus on a particular mode that propagates inwards from the boundary at the speed of light, and that can be used to apply boundary conditions adapted to the constraints. Finally, in Section VII we show two numerical examples for both a vacuum spacetime and a spacetime whose matter content is a massless scalar field, where we apply the boundary conditions introduced before. We conclude in Section VIII.

II. BSSN IN SPHERICAL SYMMETRY

We will start with a very brief discussion of the BSSN formulation [2, 3] in the particular case of spherical symmetry. The BSSN formulation is based on a conformal decomposition of the spatial metric of the form

$$\tilde{\gamma}_{ij} = e^{-4\phi} \gamma_{ij} , \quad (2.1)$$

In the standard version of this formulation, the conformal factor ϕ is chosen in such a way that the determinant of the conformal metric is unity $\tilde{\gamma} = 1$. However, this approach is ill-adapted to curvilinear coordinates where the determinant of the metric is generally different from unity even in flat space. In curvilinear coordinates it is in fact much better to ask for the determinant of the conformal metric to reduce to its value in flat space (see *e.g.* [30, 31]). If we denote the flat background metric in the chosen curvilinear coordinates by $\hat{\gamma}_{ij}$, we will then ask for $\tilde{\gamma} = \hat{\gamma}$. Moreover, we will ask for this to remain true for all times, so that $\partial_t \tilde{\gamma} = 0$, corresponding to what Brown calls a “Lagrangian” BSSN scheme [30] (for an “Eulerian” scheme one asks instead that $\tilde{\gamma}$ remains constant along normal lines, *i.e.* as seen by the Eulerian observers).¹

Associated to the conformal decomposition of the spatial metric, the BSSN formulation treats separately the trace of the extrinsic curvature K and the conformally rescaled traceless part defined as

$$\tilde{A}_{ij} := e^{-4\phi} \left(K_{ij} - \frac{1}{3} \gamma_{ij} K \right) . \quad (2.2)$$

For the particular case of spherical symmetry, we start by writing the spatial metric as

$$dl^2 = e^{4\phi} (a(r, t) dr^2 + r^2 b(r, t) d\Omega^2) , \quad (2.3)$$

with $a(r, t)$ and $b(r, t)$ positive metric functions, and $d\Omega^2$ the standard solid angle element $d\Omega^2 = d\theta^2 + \sin^2 \theta d\varphi^2$. The determinants of the physical and conformal metrics then take the form:

$$\gamma = ab^2 e^{12\phi} (r^4 \sin^2 \theta) , \quad \tilde{\gamma} = ab^2 (r^4 \sin^2 \theta) . \quad (2.4)$$

On the other hand, the determinant of the flat metric in spherical coordinates can be easily found by setting $a = b = 1$ in the expression for $\tilde{\gamma}$ above:

$$\hat{\gamma} = r^4 \sin^2 \theta . \quad (2.5)$$

The condition that $\tilde{\gamma} = \hat{\gamma}$ now implies that throughout the evolution we must have $ab^2 = 1$ (this is true for a Lagrangian evolution, for an Eulerian evolution ab^2 can in fact change in the case of a non-vanishing shift).

The evolution equations for the different dynamical quantities can be taken directly from [31]. Taking α as the lapse function and β^r as the radial component of the shift vector, we find the following evolution equation for the conformal factor:

$$\partial_t \phi = \beta^r \partial_r \phi + \frac{1}{6} \tilde{\nabla}_m \beta^m - \frac{1}{6} \alpha K , \quad (2.6)$$

with K the trace of the extrinsic curvature, and where the conformal divergence of the shift vector is given by

$$\tilde{\nabla}_m \beta^m = \partial_r \beta^r + \beta^r \left(\frac{\partial_r a}{2a} + \frac{\partial_r b}{b} + \frac{2}{r} \right) . \quad (2.7)$$

The evolution equations for the conformal metric components are

$$\partial_t a = \beta^r \partial_r a + 2a \partial_r \beta^r - \frac{2}{3} a \tilde{\nabla}_m \beta^m - 2\alpha a A_a , \quad (2.8)$$

$$\partial_t b = \beta^r \partial_r b + 2b \frac{\beta^r}{r} - \frac{2}{3} b \tilde{\nabla}_m \beta^m - 2\alpha b A_b , \quad (2.9)$$

where we A_a and A_b are defined in terms of the traceless conformal extrinsic curvature \tilde{A}_{ij} as:

$$A_a := \tilde{A}_r^r , \quad A_b := \tilde{A}_\theta^\theta . \quad (2.10)$$

Notice that since the tensor \tilde{A}_{ij} is traceless by definition, the following condition must always hold:

$$A_a + 2A_b = 0 . \quad (2.11)$$

For the trace of the extrinsic curvature K we have the following evolution equation

$$\begin{aligned} \partial_t K &= \beta^r \partial_r K - \nabla^2 \alpha + \alpha \left(A_a^2 + 2A_b^2 + \frac{1}{3} K^2 \right) \\ &+ 4\pi \alpha (\rho + S_a + 2S_b) , \end{aligned} \quad (2.12)$$

¹ One can account for both cases by introducing an extra parameter σ as in Ref. [31]. For this analysis we limit ourselves to the Lagrangian case $\sigma = 1$.

with ρ the energy density of matter, and S_a and S_b are the mixed components of the stress tensor: $S_a = S_r^r$, $S_b := S_\theta^\theta$. Notice also that the Laplacian of the lapse that appears above is with respect to the physical metric, and takes the form

$$\nabla^2 \alpha = \frac{1}{ae^{4\phi}} \left[\partial_r^2 \alpha - \partial_r \alpha \left(\frac{\partial_r a}{2a} - \frac{\partial_r b}{b} - 2\partial_r \phi - \frac{2}{r} \right) \right]. \quad (2.13)$$

For the traceless part of the conformal extrinsic curvature we first notice that in fact we only need an evolution equation for A_a , since the traceless condition implies $A_b = -A_a/2$. We have

$$\begin{aligned} \partial_t A_a &= \beta^r \partial_r A_a - \left(\nabla^r \nabla_r \alpha - \frac{1}{3} \nabla^2 \alpha \right) + \alpha \left(R_r^r - \frac{1}{3} R \right) \\ &+ \alpha K A_a - \frac{16}{3} \pi \alpha (S_a - S_b), \end{aligned} \quad (2.14)$$

where now

$$\nabla^r \nabla_r \alpha = \frac{1}{ae^{4\phi}} \left[\partial_r^2 \alpha - \partial_r \alpha \left(\frac{\partial_r a}{2a} + 2\partial_r \phi \right) \right]. \quad (2.15)$$

A crucial part of the BSSN formulation is how we write the components of the Ricci tensor that appear in Eq. (2.14) above. For BSSN in spherical symmetry we write

$$\begin{aligned} R_r^r &= -\frac{1}{ae^{4\phi}} \left[\frac{\partial_r^2 a}{2a} - a \partial_r \Delta^r - \frac{3}{4} \left(\frac{\partial_r a}{a} \right)^2 \right. \\ &+ \frac{1}{2} \left(\frac{\partial_r b}{b} \right)^2 - \frac{1}{2} \Delta^r \partial_r a + \frac{\partial_r a}{rb} + 2\lambda \left(1 + \frac{r \partial_r b}{b} \right) \\ &\left. + 4 \partial_r^2 \phi - 2 \partial_r \phi \left(\frac{\partial_r a}{a} - \frac{\partial_r b}{b} - \frac{2}{r} \right) \right], \quad (2.16) \\ R &= -\frac{1}{ae^{4\phi}} \left[\frac{\partial_r^2 a}{2a} + \frac{\partial_r^2 b}{b} - a \partial_r \Delta^r - \left(\frac{\partial_r a}{a} \right)^2 \right. \\ &+ \frac{1}{2} \left(\frac{\partial_r b}{b} \right)^2 + \frac{2}{rb} \left(3 - \frac{a}{b} \right) \partial_r b \\ &+ 4\lambda + 8 \left(\partial_r^2 \phi + (\partial_r \phi)^2 \right) \\ &\left. - 8 \partial_r \phi \left(\frac{\partial_r a}{2a} - \frac{\partial_r b}{b} - \frac{2}{r} \right) \right]. \quad (2.17) \end{aligned}$$

where $\lambda := (1 - a/b)/r^2$ is a variable used for the regularization of the origin (but that here we will use just as a shorthand), and where we have introduced the “connection vector” Δ^i , which is defined in terms of the Christoffel symbols of the conformal metric $\tilde{\Gamma}_{mn}^i$ and those of the flat background metric $\tilde{\Gamma}_{mn}^i$ as

$$\Delta^i = \tilde{\gamma}^{mn} \left(\tilde{\Gamma}_{mn}^i - \tilde{\Gamma}_{mn}^i \right). \quad (2.18)$$

Being defined as a difference of Christoffel symbols, Δ^i is in fact a true vector. In spherical symmetry the only non-trivial component is Δ^r , which takes the explicit form

$$\Delta^r = \frac{1}{a} \left(\frac{\partial_r a}{2a} - \frac{\partial_r b}{b} - 2r\lambda \right). \quad (2.19)$$

In the BSSN formulation, Δ^r is now promoted to an independent variable. Its evolution equation is obtained from its definition above, but it is then modified using the momentum constraint to eliminate the divergence of the traceless extrinsic curvature. In the particular case of spherical symmetry one then finds

$$\begin{aligned} \partial_t \Delta^r &= \beta^r \partial_r \Delta^r - \Delta^r \partial_r \beta^r + \frac{1}{a} \partial_r^2 \beta^r + \frac{2}{b} \partial_r \left(\frac{\beta^r}{r} \right) \\ &+ \frac{1}{3} \left(\frac{1}{a} \partial_r (\tilde{\nabla}_m \beta^m) + 2\Delta^r \tilde{\nabla}_m \beta^m \right) \\ &- \frac{2}{a} (A_a \partial_r \alpha + \alpha \partial_r A_a) + 2\alpha \left(A_a \Delta^r - \frac{2r}{b} A_\lambda \right) \\ &+ \frac{\alpha \xi}{a} \left[\partial_r A_a - \frac{2}{3} \partial_r K + 6A_a \partial_r \phi \right. \\ &\left. + r^2 A_\lambda \left(\frac{2}{r} + \frac{\partial_r b}{b} \right) - 8\pi j_r \right], \end{aligned} \quad (2.20)$$

with $A_\lambda := (A_a - A_b)/r^2$ another regularization variable that we only use here as a shorthand, j_r the (physical) covariant component of the momentum density, and where ξ is an arbitrary parameter such that $\xi > 1/2$, with the value $\xi = 2$ corresponding to standard BSSN.

Our final system of evolution equations is then given by equations (2.6), (2.8), (2.9), (2.12), (2.14) and (2.20).

Before finishing this section, it is also convenient to write the specific form of the Hamiltonian and momentum constraints. One finds

$$H := R - (A_a^2 + 2A_b^2) + \frac{2}{3} K^2 - 16\pi\rho = 0, \quad (2.21)$$

$$\begin{aligned} M &:= \partial_r A_a - \frac{2}{3} \partial_r K + 6A_a \partial_r \phi \\ &+ r^2 A_\lambda \left(\frac{2}{r} + \frac{\partial_r b}{b} \right) - 8\pi j_r = 0. \end{aligned} \quad (2.22)$$

One should also remember that, since we have promoted the quantity Δ^r to an independent variable, we in fact have another constraint corresponding to the definition of Δ^r , namely

$$C_\Delta := a\Delta^r - \left(\frac{\partial_r a}{2a} - \frac{\partial_r b}{b} - 2r\lambda \right) = 0. \quad (2.23)$$

III. CHARACTERISTIC STRUCTURE OF THE EVOLUTION EQUATIONS

The first step in constructing our boundary conditions is to study the characteristic structure of the system of evolution equations given above. We will do this very

schematically, the details for the general case with no spherical symmetry can be found in [32].

Our system of evolution equations is first order in time but second order in space, so we start by introducing the following auxiliary quantities

$$q := \partial_r \ln \alpha, \quad \chi := \partial_r \phi, \quad (3.1)$$

$$d_a := \frac{1}{2} \partial_r \ln a, \quad d_b := \frac{1}{2} \partial_r \ln b. \quad (3.2)$$

We will also assume that the radial component of the shift vector β^r is an a priori known function of spacetime. For the lapse, on the other hand, we will assume a Bona-Masso slicing condition of the form [33]

$$\partial_t \alpha - \beta^r \partial_r \alpha = -\alpha^2 f(\alpha) K, \quad (3.3)$$

with $f(\alpha) > 0$ an arbitrary positive function of α .

With these considerations we find that, up to principal part (higher derivatives), the system of evolution equations of the previous Section becomes

$$\partial_0 q \simeq -\alpha f \partial_r K, \quad (3.4)$$

$$\partial_0 \chi \simeq -\frac{1}{6} \alpha \partial_r K + \frac{\beta^r}{6} \partial_r (d_a + 2d_b), \quad (3.5)$$

$$\partial_0 d_a \simeq -\alpha \partial_r A_a - \frac{\beta^r}{3} \partial_r (d_a + 2d_b), \quad (3.6)$$

$$\partial_0 d_b \simeq -\alpha \partial_r A_b - \frac{\beta^r}{3} \partial_r (d_a + 2d_b), \quad (3.7)$$

$$\partial_0 K \simeq -\frac{\alpha}{ae^{4\phi}} \partial_r q, \quad (3.8)$$

$$\partial_0 A_a \simeq -\frac{2\alpha}{3ae^{4\phi}} \partial_r (q + d_a - d_b + 2\chi - a\Delta^r), \quad (3.9)$$

$$\partial_0 \Delta^r \simeq -\frac{4\alpha}{3a} \partial_r K + \frac{\beta^r}{3a} \partial_r (d_a + 2d_b), \quad (3.10)$$

where we have defined $\partial_0 := \partial_t - \beta^r \partial_r$, and where the symbol \simeq denotes “equal up to principal part”. For simplicity, we have also already restricted ourselves to the standard BSSN choice $\xi = 2$ (the more general case can be easily considered, but it is not needed for our present purposes). In order to close the system we should also give the evolution equations of the lower order terms a , b , α and ϕ , but those evolution equations don’t involve spatial derivatives of the dynamical variables so that they turn out to be trivial up to principal part.

From the structure of the equations above we can immediately see that there is a mode that does not propagate at all, namely:

$$\omega^d := d_a + 2d_b. \quad (3.11)$$

This is not surprising since we started the discussion assuming a Lagrangian BSSN scheme characterized by $\partial_t \tilde{\gamma} = 0$, and the above combination is the precisely dynamical part of $\partial_r \tilde{\gamma}$ (if one considers an Eulerian scheme this eigenfield propagates in the normal direction with speed $-\beta^r$). This eigenfield is not usually discussed since for the standard BSSN formulation in Cartesian-like coordinates one assumes that $\tilde{\gamma} = 1$, so that its spatial

derivatives vanish. By relaxing this assumption we now find that this eigenfield must be considered in the analysis, and its propagation properties will depend on the way in which the conformal volume element is assumed to evolve.

Proceeding with the analysis, we find two eigenfields that propagate along the normal lines with speed $-\beta^r$. They are

$$\omega^q := q - 6f\chi - f(d_a + 2d_b), \quad (3.12)$$

$$\omega^\Delta := \Delta^r - 8\chi/a - (d_a + 2d_b)/a. \quad (3.13)$$

We can also identify two propagating eigenfields associated with the slicing condition, they are

$$\omega_\pm^\alpha = e^{2\phi} \sqrt{af} K \pm q, \quad (3.14)$$

and they propagate with the characteristic speeds:

$$\lambda_\pm^\alpha = -\beta^r \pm \alpha e^{-2\phi} \sqrt{f/a}. \quad (3.15)$$

Notice that this speed depends on the slicing choice through the function $f(\alpha)$ (it is a “gauge” speed), and can easily be larger than the speed of light without any physical consequences (this in fact happens whenever $f > 1$).

The last two eigenfields are:

$$\begin{aligned} \omega_\pm^l &= e^{2\phi} \sqrt{a} \left(A_a - \frac{2}{3} K \right) \\ &\pm \frac{2}{3} (d_a - d_b - a\Delta^r + 2\chi), \end{aligned} \quad (3.16)$$

and propagate with the speeds:

$$\lambda_\pm^l = -\beta^r \pm \alpha e^{-2\phi} \sqrt{1/a}, \quad (3.17)$$

which are nothing more than the local coordinate speed of light for outward and inward moving light rays. Since these last two modes propagate with the speed of light one could be tempted to think that they are related to gravitational waves, but they are not. Remember that we are in spherical symmetry so there are no gravitational waves. In fact, these modes propagate at the speed of light only because we have chosen standard BSSN with $\xi = 2$, any other choice results in a different propagation speed. These modes are related to the way in which the momentum constraint is added to the evolution equation for Δ^r , so we should expect them to be related to the violation of the constraints at the boundary.

It is important to mention that for the propagating eigenfields in equations (3.14) and (3.16), the plus sign corresponds to modes propagating to the right, that is “outgoing” modes, while the minus sign corresponds to modes propagating to the left, i.e. “incoming” modes. One could naively think that a good boundary condition would be to simply fix the incoming modes at the boundary to zero, but this is not the case. As we will see below in Section V, even for the gauge modes the fact that the

outgoing modes behave as spherical waves that fall off as $1/r$ implies that the incoming mode does not vanish at the boundary. For the modes propagating at the speed of light (3.16) the situation is even more complicated, since, as we will show in Section VI, the constraints fix the form of the incoming mode to something highly non-trivial.

A final remark is in order before starting the discussion of boundary conditions. We evolve numerically the BSSN system formulated as a PDE system that is first order in time and second order in space, as discussed in Section II. As such we cannot apply boundary conditions directly to the eigenfields, but only to the original dynamical variables. Still, the knowledge of the characteristic structure allows us to introduce well behaved and consistent boundary conditions, as will be discussed below.

IV. BOUNDARY CONDITIONS FOR THE NON-PROPAGATING EIGENFIELDS

From here on we will assume for simplicity that the shift vector vanishes at the boundary (in modern simulations of isolated systems this is generally not true, but the shift is still usually very small at the boundary so that this is not a bad approximation). Under this assumption the time and normal direction coincide, so we may consider the case of the eigenfields that propagate along the time and normal lines in this Section.

We may distinguish two types of eigenfields: the one that propagates along the time direction, corresponding to the combination

$$\omega^d := d_a + 2d_b, \quad (4.1)$$

and the ones that propagate along the normal direction, i.e. those with characteristic speed equal to $-\beta^r$. In our case these correspond to the following two combinations of q , χ , Δ^r , d_a and d_b :

$$\omega^q := q - 6f\chi - f(d_a + 2d_b), \quad (4.2)$$

$$\omega^\Delta := \Delta^r - 8\chi/a - (d_a + 2d_b)/a. \quad (4.3)$$

While the first one never propagates regardless of the behavior of the other variables, for a vanishing shift the remaining two fields also do not propagate, so that one can in principle evolve all of them directly at the boundary.

Notice that q , χ , d_a and d_b are in fact auxiliary quantities (spatial derivatives of metric components) that are not evolved directly in the BSSN formulation. We have found that in practice one can simply evolve α , ϕ , a and b all the way to the boundary without applying any special boundary condition to them. For the case of a vanishing shift at the boundary, the evolution equations for these quantities do not involve any spatial derivatives, so evolving all the way to the boundary is trivial.

This leaves us with the task of applying a boundary condition for Δ^r . We have in fact tried two different approaches:

1. The simplest approach is to just evolve Δ^r all the way to the boundary, using one-sided differences for the radial derivatives of α and K that appear in its evolution equation (2.20) (remember that we are taking $\xi = 2$).
2. The other possibility is to reconstruct the non-propagating field ω^Δ at the boundary in the old time level, evolve it directly to the new time level, and then solve for Δ^r using the fact that we have already updated a , b and ϕ so that we can calculate their radial derivatives in the new time level using one-sided differences.

Both these methods allow us to have stable and convergent evolutions, and in fact seem to give almost identical results. But the second method is more complicated to code, so that in practice we prefer the first. In summary, in the case of vanishing shift, the non-propagating eigenfields can be dealt with in a simple way by just evolving α , ϕ , a , b and Δ^r all the way to the boundary, using one-sided differences for the spatial derivatives that appear in the evolution equation for Δ^r .

V. BOUNDARY CONDITIONS FOR THE GAUGE EIGENFIELDS

Next let us consider the gauge eigenfields:

$$\omega_\pm^\alpha = e^{2\phi} \sqrt{af} K \pm q, \quad (5.1)$$

which propagate with the speeds $\lambda_\pm^\alpha = \pm \alpha e^{-2\phi} \sqrt{f/a}$ (again assuming a vanishing shift). Clearly, one of the eigenfields propagates outward while the other propagates inward. In order to respect causality one can then only give a boundary condition for the incoming eigenfield. An obvious choice would be to simply set the incoming field to zero at the boundary. This would work well in the case of plane waves in Cartesian coordinates, but produces noticeable reflections at the boundary for the case of spherical waves that decay as $1/r$.

We then take a different approach and assume that asymptotically the lapse function behaves as a spherical wave. This follows from the fact that when combining equations (2.12) and (3.3) the resulting equation for the lapse (assuming a vanishing shift) is a wave equation of the form

$$\partial_t^2 \alpha - \alpha^2 f \nabla^2 \alpha = \alpha^3 f \left[K^2 \left(2f + \alpha f' - \frac{1}{3} \right) - \frac{3}{2} A_a^2 + 4\pi (\rho + S) \right]. \quad (5.2)$$

In the asymptotic region one expects the right hand side to be negligible, so we may safely assume that in an asymptotically flat scenario the lapse behaves for large r as

$$\alpha \simeq 1 + g(r - vt)/r, \quad (5.3)$$

with g some unknown function, and $v = \alpha e^{-2\phi} \sqrt{f/a}$. This condition can be imposed as a Sommerfield type condition of the form:

$$(\partial_t + v \partial_r) [r(\alpha - 1)] \simeq 0, \quad (5.4)$$

which can be seen, by substituting (3.3), to be equivalent to having a non-vanishing incoming eigenfield given by

$$\omega_-^\alpha \simeq (\alpha - 1) / r, \quad (5.5)$$

quite independently of the form of the function g .

So, for our boundary condition we then first update α all the way to the boundary, find ω_-^α from the above expression, calculate $q = \partial_r(\ln \alpha)$ at the boundary using one-sided differences, and finally solve for K from the definition of ω_-^α :

$$K = \frac{\omega_-^\alpha + q}{e^{2\phi} \sqrt{af}}. \quad (5.6)$$

The above procedure is consistent since we are only allowed to apply a boundary condition for the incoming eigenfield, and we are using this to solve for K . In practice we have found that this boundary condition is quite robust and stable, and results in very small reflections at the boundary which become even smaller as the boundary is pushed further away.

As a final comment we should mention that since this is a pure gauge sector, any boundary condition we choose for the incoming eigenfield would in fact be physically consistent. Still, minimizing boundary reflections is desirable as we would then remain in essentially the same gauge if we move the position of the boundaries.

VI. CONSTRAINT PRESERVING BOUNDARY CONDITION

In the previous Section we discussed how to apply boundary conditions for the gauge eigenfields that are mathematically consistent in the sense that they respect causality, which results in the simple prescription of allowing the outgoing eigenfield to leave the grid undisturbed, and choosing boundary data only for the incoming eigenfield. We also showed how one can choose this incoming data in a way that is consistent with having spherical outgoing waves, and how in such a case just setting the incoming fields to zero is not correct.

One could try to use the same idea for the case of the remaining eigenfields (3.16). It turns out, however, that having boundary data that respects causality is not enough since in general relativity we also have to make sure that the constraints are satisfied at the boundary, and in order for this to be true one can not choose the incoming field freely. The first thing to notice is that we can in fact construct both the radial and the time derivatives of the eigenfields ω_\pm^l up to principal part as a combination of constraints. For example, by starting

from eq. (3.16), taking a radial derivative, and rearranging terms one can show that:

$$\partial_r \omega_\pm^l = \sqrt{a} e^{2\phi} M \mp \left(\frac{a e^{4\phi} H}{6} + \frac{\partial_r C_\Delta}{2} \right) + P_\pm, \quad (6.1)$$

with H , M and C_Δ the Hamiltonian, momentum and Delta constraint defined earlier, and where P_\pm is a source term that involves only first derivatives of the metric components and undifferentiated components of the extrinsic curvature, whose explicit form is somewhat long and not particularly illuminating so we will not write it here (but it is not difficult to find it using an algebraic computational package). The above relation is not surprising since the combinations of constraints appearing on the right-hand side of (6.1) correspond precisely to the eigenfields of the constraint subsystem (see Appendix A). Imposing now the condition that the incoming constraint eigenfield should vanish, we can reduce the last equation (taking the minus sign) to:

$$\partial_r \omega_-^l = P_- . \quad (6.2)$$

Similarly, one can take instead a time derivative of ω_\pm^l , use of the evolution equations of the different dynamical quantities, and rearrange terms to find

$$\begin{aligned} \partial_t \omega_\pm^l &= \left(\beta^r \mp \frac{\alpha}{\sqrt{a} e^{2\phi}} \right) \left[\sqrt{a} e^{2\phi} M \right. \\ &\quad \left. \mp \left(\frac{a e^{4\phi} H}{6} + \frac{\partial_r C_\Delta}{2} \right) \right] + Q_\pm, \end{aligned} \quad (6.3)$$

where as before Q_\pm are sources that involve only lower order terms. Imposing again that the incoming constraint eigenfield vanishes we find:

$$\partial_t \omega_-^l = Q_- . \quad (6.4)$$

Notice that equations (6.1) and (6.3) can in fact be combined to yield:

$$\begin{aligned} \partial_t \omega_\pm^l + \left(-\beta^r \pm \frac{\alpha}{\sqrt{a} e^{2\phi}} \right) \partial_r \omega_\pm^l \\ = Q_\pm + \left(-\beta^r \pm \frac{\alpha}{\sqrt{a} e^{2\phi}} \right) P_\pm, \end{aligned} \quad (6.5)$$

which of course just confirms the fact that ω_+^l and ω_-^l are indeed outgoing and incoming fields respectively.

The above results suggest two different approaches for imposing a boundary condition on the incoming field ω_-^l :

1. Radial derivative method: Calculate the value of the source term P_- at the new time level close to the boundary (typically one grid point in), using the local evolved values of the extrinsic curvature and numerical radial derivatives of the metric components (which can easily be calculated since the metric components are evolved all the way to the

boundary). Use this value of P_- to obtain $\partial_r \omega_-^l$ close to the boundary, and solve for the value of ω_-^l at the boundary using equation (6.2) and a finite difference approximation to the derivative. For example, if the boundary is located at the grid point N , and we are using a second order finite difference approximation, we first calculate $P_-(N-1)$, and use this to obtain $\omega_-^l(N)$ as follows

$$\omega_-^l(N) = \omega_-^l(N-2) + 2P_-(N-1) \Delta r . \quad (6.6)$$

Finally, once we have ω_-^l at the boundary we can simply use equation (3.16) to solve for the boundary value of A_a , knowing already the boundary values of K , Δ^r and the different metric components (from which one can calculate their radial derivatives using one-sided differences).

2. **Time derivative method:** Calculate the value of the source term Q_- at the boundary at the same time as we calculate the time derivatives of all other fields, using one-sided radial derivatives when needed. Use equation (6.4) to evolve ω_-^l at the boundary for one time step at the same time as all other dynamical fields. Finally, solve for the boundary value of A_a from (3.16).

Both these methods are quite easy to code, though the method based on the time derivative is conceptually simpler and one could expect it to give more accurate results. At first sight, it could seem there is a lack of consistency since both source terms P_- and Q_- depend explicitly on A_a , and we are using them to determine precisely the value of A_a at the boundary. However, notice that in the space derivative method we actually just calculate P_- at points close to the boundary and never at the boundary itself, while for the time derivative method we calculate Q_- at the previous time level, so that in both cases there is no reference to the boundary value of A_a at the new time level in the calculation of the source terms.

One could also be worried about the fact that we have simply imposed the condition that the incoming constraint eigenfield is zero, by assuming that the combinations appearing in equations (6.1) and (6.3) (with the minus sign) are equal to zero. This approach is perfectly consistent since we allow the outgoing constraint mode to propagate freely through the boundary. Moreover, while fixing the incoming constraint eigenfield to zero may not be the optimal choice, this only introduces small reflections of the constraints at the boundaries that converge to zero as the resolution is increased.

VII. SOME NUMERICAL EXAMPLES

In the previous sections we have discussed how to apply boundary conditions to the different fields that respect causality and also guarantee that no violations of the

constraints will be introduced at the boundaries. Here we will show a few numerical examples of these boundary conditions at work.

All the simulations presented below were performed with a numerical code that solves the BSSN system in spherical symmetry, using a method of lines with a fourth order Runge-Kutta time integrator, fourth order centered spatial differences for the interior, and fifth order one-sided differences at the boundary. The origin is staggered, with symmetry and regularity conditions imposed as described in [31]. In particular, we report the results using the first method proposed in Section IV for the non-propagating fields, and omit the other choice since we find no noticeable difference. Our simulations were performed on a numerical domain that goes from $r = 0$ to $r = 25$, using three different resolutions for convergence analysis, $\Delta r = 0.1, 0.0707, 0.05$, with corresponding grids of 250, 354 and 500 spatial points (these values were chosen in order to refine the discretization interval by a factor of $\sqrt{2}$). In each simulation the time step was chosen such that $\Delta t = \Delta r/2$.

A. Pure gauge dynamics

As a first example we will consider the evolution of Minkowski spacetime with a non-trivial foliation. For this evolution we will make use of the so-called harmonic slicing condition, which can be written in the form

$$\partial_t \alpha = -\alpha^2 K . \quad (7.1)$$

Notice that this is a particular case of the Bona-Masso family of slicing conditions (3.3) with $f(\alpha) = 1$ (remember that we are using a vanishing shift vector). One consequence of this particular choice is that the gauge eigenfields ω_\pm^α now propagate with the same speed as the modes ω_\pm^l , namely the coordinate speed of light.

As initial conditions we take a flat slice of Minkowski spacetime such that

$$\begin{aligned} a = b &= 1 , \\ K = A_a &= 0 , \\ \phi &= 0 , \\ \Delta^r &= 0 , \end{aligned}$$

The only way to obtain a non-trivial evolution is to choose a non-trivial initial lapse. We will then take the initial lapse to have the following Gaussian profile

$$\alpha = 1 + \alpha_0 \left\{ e^{-\left(\frac{r-r_0}{\sigma_0}\right)^2} + e^{-\left(\frac{r+r_0}{\sigma_0}\right)^2} \right\} , \quad (7.2)$$

where the reflected Gaussian is included in order to have the right parity behavior of the lapse function at the origin, as demanded by the symmetry considerations. In this expression α_0 is the amplitude of the Gaussian, r_0 its initial position and σ_0 controls the width. For the simulation shown below we have used the parameters $\alpha_0 = 0.01$,

$r_0 = 5.0$ and $\sigma_0 = 1.0$; the initial lapse profile is shown in the first panel of Figure 1.

We follow the evolution of this initial data in Figure 1. Because we are taking $K = 0$ initially, the initial Gaussian pulse in the lapse splits into two smaller pulses moving in opposite directions. The incoming pulse grows as it approaches the origin, where it inverts in sign and starts moving out (panel 2), later both pulses move out with their amplitude decaying as $1/r$ and eventually leave the numerical domain (panels 3 and 4). The other dynamical fields react accordingly, giving a non-trivial geometry to the spatial slices at each new time step. The boundary conditions applied minimize spurious reflections when the pulses reach the boundary, and the simulation can continue for periods of time much greater than the light crossing time of the computational domain, while keeping the simulation accurate and stable.

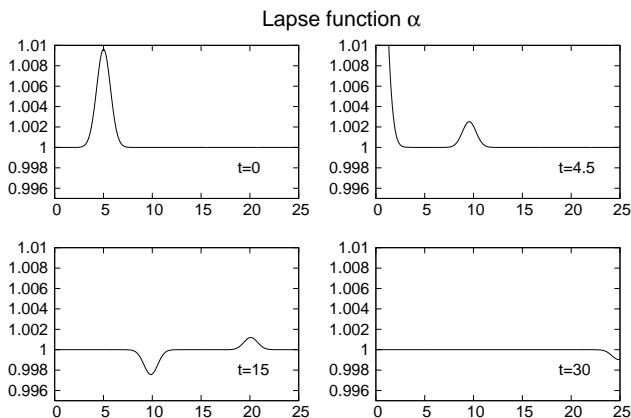


FIG. 1: Snapshots of the evolution of the lapse α . The panels correspond to times $t = 0, 4.5, 15, 30$.

We may further analyze the behavior of the evolution as the propagating modes reach the outer boundary. First we turn to the radial derivative method discussed in Section VI. Figures 2 and 3 show the numerical evolution of the Hamiltonian and momentum constraints for the three resolutions employed. Of course, since the evolution system propagates the constraints, the fact that they do not remain equal to zero is only due to numerical truncation error. As mentioned before, for all our simulations both the spatial discretization and time integration were done at fourth order. This means that when the resolution is doubled, the values of the constraints should go down by a factor of $2^4 = 16$. In the plots we rescale the different resolutions by the corresponding factors expected for fourth order convergence, so that for a convergent simulation the different lines should lie on top of each other.

The first two panels of figures 2 and 3 show the early evolution up to moments prior to the time when the outgoing pulses reach the boundary. The convergence of the interior evolution is evident since the numerical value of the constraints scales consistently with the fourth order

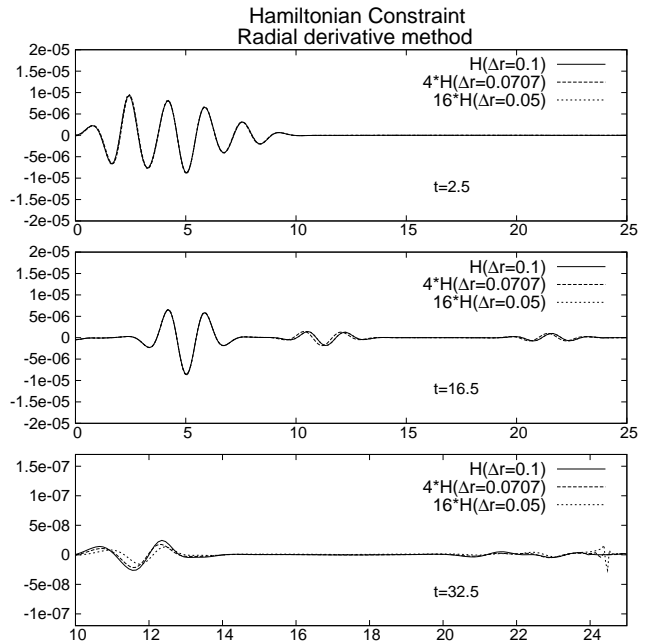


FIG. 2: Evolution of the Hamiltonian constraint when applying the radial derivative method discussed in the text. The higher resolutions have been rescaled by factors of 4 and 16 to show the convergence of the solution to fourth order (the ratio between subsequent resolutions is $\sqrt{2}$). In the last panel the radial axis has been shifted and the vertical axis rescaled in order to better appreciate the reflected pulses.

discretization. As mentioned in Section III, in the BSSN formulation there are some modes that do not propagate. This is made evident on the plots of the Hamiltonian constraint, where after the initial pulses propagate away there is always a non-zero remnant at the position of the initial Gaussian pulse in the lapse (this is essentially caused by the mode ω^d). The third panel of both Figures shows the value of the constraints some time after both outgoing pulses have passed through the boundary. Notice that in the third panel of both Figures the radial axis has been shifted, and the vertical axis rescaled, in order to better observe the reflections induced by the boundaries. The first thing to notice is that there are indeed reflections of the constraints at the boundary, and those reflections are much lower in amplitude (about two orders of magnitude) than the outgoing pulses that reached the boundary. Also, the amplitude of those reflections is smaller as we increase the resolution, and they converge to zero at the expected fourth order. We can also appreciate a slight phase shift in the reflected pulses which is a consequence of the grid structure employed: since we stagger the origin for regularization purposes the position of the boundaries does not exactly coincide (for a given resolution it is shifted $\Delta r/2$ outside of the previous resolution). We didn't include any higher resolutions since when doubling the highest resolution shown here the truncation error becomes comparable with the size

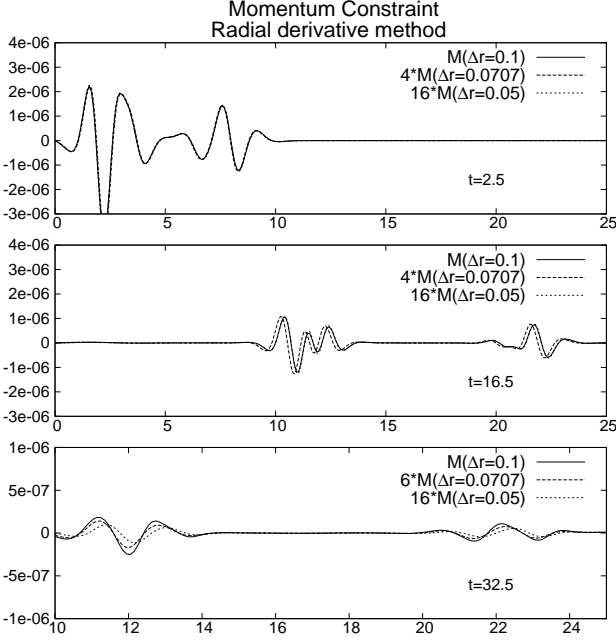


FIG. 3: Evolution of the momentum constraint when applying the radial derivative method discussed in the text. The lines are rescaled as in the plot of the Hamiltonian constraint. In the last panel the radial axis has been shifted and the vertical axis rescaled in order to better appreciate the reflected pulses.

of the machine round-off error.

We now turn to the simulation of the same initial data, but now using the time derivative method as discussed in Section VI. The evolution proceeds in a very similar way to the previous case, with very small numerical reflections at the boundaries that converge to zero as the resolution is increased. The evolution of the Hamiltonian and momentum constraints is shown in Figures 4 and 5 for the three different resolutions used. As before, the first two panels of those figures correspond to times prior to the arrival of the pulses at the boundary, while the third panel shows the situation some time after the pulses have reached the boundary. Again, we can see that there are small reflections. As we increase the resolution, the matching of the rescaled profiles improves, showing that the violation of the constraints reflected at the boundaries converges to zero to fourth order. The amplitude of the reflections seems to be somewhat larger than in the previous case (this is more evident in the momentum constraint), but as the resolution is increased both methods seem to give very similar results.

In order to get an idea of how much better our boundary conditions behave when compared to the more standard “outgoing wave” boundary conditions, we show in Figure 6 the value of the Hamiltonian constraint at different times using the following boundary condition for the different dynamical variables:

$$(\partial_t + v\partial_r)[r(u - u_0)] = 0, \quad (7.3)$$

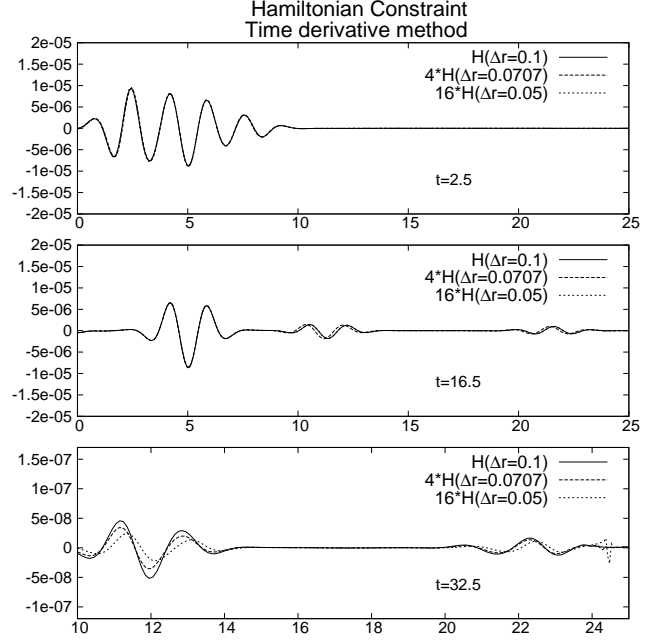


FIG. 4: Evolution of the Hamiltonian constraint when applying the time derivative method discussed in the text. The higher resolutions have been rescaled by factors of 4 and 16 to show the convergence of the solution to fourth order (the ratio between subsequent resolutions is $\sqrt{2}$). In the last panel the radial axis has been shifted and the vertical axis rescaled in order to better appreciate the reflected pulses.

where u represents a given dynamical variable, u_0 its asymptotic value, and v the asymptotic characteristic speed (which in this case is just 1 for all fields). In order to not over-determine the system at the boundary, the above boundary condition is only applied to the variables K and A_a , while all order variables are evolved up to the boundary using one-sided differences when necessary. Apart from the different outer boundary condition, all the other parameters are identical to the simulations described above. The first panel shows the situation at $t = 2.5$ when boundary effects are not yet relevant. This should be compared with the first panel of Figures 2 and 4, but notice that now we do not rescale the higher resolutions. We clearly see that the Hamiltonian converges consistently to zero on the interior points of the domain. The situation changes once the outgoing pulses reach the boundary, as can be seen in the second panel of Figure 6 which shows the situation at $t = 32.5$, and should be compared with the third panel of Figures 2 and 4 (but notice the change in scales). From the comparison it is clear that the reflected constraint violations are much larger than in the previous cases, by several orders of magnitude, and also that they do not converge to zero as the resolution is increased. The last panel of Figure 6 shows the situation at $t = 45$, once the reflections have reached the origin. Even if the simulation remains stable and well behaved, the large constraint violations

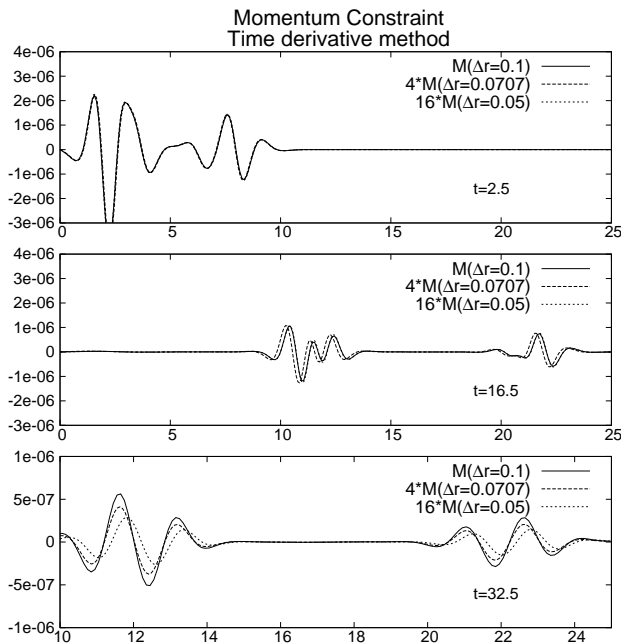


FIG. 5: Evolution of the momentum constraint when applying the time derivative method discussed in the text. The graphs are rescaled as in the plot of the Hamiltonian constraint showing fourth order convergence. In the last panel the radial axis has been shifted and the vertical axis rescaled in order to better appreciate the reflected pulses.

introduced at the boundary now affect the whole numerical domain and, since they don't converge to zero, will not allow us to recover accurately the correct physical solution even in the continuum limit. It is precisely for this reason that simulations using this standard boundary conditions must place the boundaries as far away as possible. We can then conclude that, even for this simple case, our set of constraint adapted boundary conditions shows a great improvement over the standard “outgoing wave” conditions usually employed in numerical simulations.

B. Scalar field

1. Evolution equations and boundary conditions

For our second example we now consider a truly dynamical scenario that corresponds to a spacetime whose matter content is a massless scalar field. The propagation of a spherically symmetric distribution of a massless scalar field has been well studied in the past, and depending on the initial data the final stage corresponds to one of two possible outcomes: for weak data the scalar field disperses away to infinity, while for stronger data it collapses to form a black hole [34]. For our purposes it is enough to concentrate on the non-collapsing case since

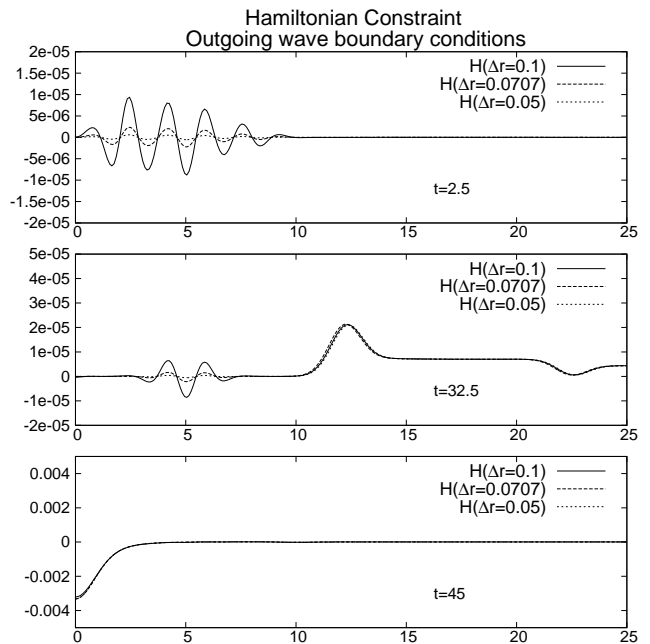


FIG. 6: Evolution of the Hamiltonian constraints for a standard “outgoing wave” boundary condition (this Figure should be compared with Figures 2 and 4). The values are not rescaled as in the previous cases in order to show that, once the boundary effects become relevant, constraint violations that do not converge to zero propagate inward throughout the whole numerical domain.

we are focusing on the interaction at the outer boundary.

For this case we also need to take into account the effect of the boundary conditions applied to the scalar field. As before, we choose a vanishing shift vector. For the lapse function we will now choose the standard “1+log” slicing, which corresponds to (3.3) with $f(\alpha) = 2/\alpha$

$$\partial_t \alpha = -2\alpha K. \quad (7.4)$$

The reason for choosing 1+log instead of harmonic slicing is two-fold: First, 1+log slicing is widely used in numerical relativity so we believe that it is important to show one example that uses it, and second, since the asymptotic gauge speed is now $\sqrt{2}$ instead of 1, this example also shows that our boundary conditions behave well also in a case when not all propagating fields do so at the same speed.

The matter coupling and the dynamics of the scalar field can be obtained from its stress-energy tensor

$$T_{\mu\nu} = \partial_\mu \Phi \partial_\nu \Phi - \frac{1}{2} g_{\mu\nu} \partial^\alpha \Phi \partial_\alpha \Phi. \quad (7.5)$$

The conservation equation $T^{\mu\nu}{}_{;\nu} = 0$ implies that the scalar field obeys the wave equation $\square \Phi = 0$. Since the terms that couple to the BSSN equations are quadratic on first derivatives, the hyperbolic structure of the geometric sector is unaltered. In order to rewrite the wave equation

for the scalar field as a first order system in spherical symmetry we first define the quantities:

$$\Pi := n^\mu \partial_\mu \Phi = \frac{1}{\alpha} \partial_t \Phi, \quad (7.6)$$

$$\Psi := \partial_r \Phi. \quad (7.7)$$

In terms of these quantities, the matter terms that couple to the BSSN equations are

$$\rho := \frac{1}{2} \left(\Pi^2 + \frac{\Psi^2}{ae^{4\phi}} \right), \quad (7.8)$$

$$j^r := -\Pi\Psi, \quad (7.9)$$

$$S_a := \frac{1}{2} \left(\Pi^2 + \frac{\Psi^2}{ae^{4\phi}} \right), \quad (7.10)$$

$$S_b := \frac{1}{2} \left(\Pi^2 - \frac{\Psi^2}{ae^{4\phi}} \right). \quad (7.11)$$

The wave equation rewritten in terms of the first order variables takes the form:

$$\partial_t \Phi = \alpha \Pi, \quad (7.12)$$

$$\partial_t \Psi = \partial_r (\alpha \Pi), \quad (7.13)$$

$$\begin{aligned} \partial_t \Pi = & \frac{\alpha}{ae^{4\phi}} \left[\partial_r \Psi + \Psi \left(\frac{2}{r} - \frac{\partial_r a}{2a} + \frac{\partial_r b}{b} + 2\partial_r \phi \right) \right] \\ & + \frac{\Psi}{ae^{4\phi}} \partial_r \alpha + \alpha K \Pi. \end{aligned} \quad (7.14)$$

Up to principal part the above system just consists on the terms that contain first derivatives of Ψ and Π . We then find that the eigenfields associated to the scalar field ω_\pm^Φ , and their corresponding eigenspeeds λ_\pm^Φ , are given by

$$\omega_\pm^\Phi = \Pi \mp \frac{\Psi}{e^{2\phi}\sqrt{a}}, \quad \lambda_\pm^\Phi = \pm \frac{\alpha}{e^{2\phi}\sqrt{a}}. \quad (7.15)$$

We will again use these modes to impose our boundary conditions. The scalar field Φ is now an auxiliary variable that doesn't propagate, so integrating its evolution equation all the way up to the boundary is adequate. Again, just setting the incoming eigenfield equal to zero is not a good idea since we are in spherical symmetry. Instead we assume that the scalar field behaves asymptotically as a spherical wave of the form:

$$\phi \simeq g(r - vt)/r, \quad (7.16)$$

with g some arbitrary function and $v = \alpha e^{-2\phi}/\sqrt{a}$. This can be shown to imply that the incoming field ω_-^Φ behaves as:

$$\omega_-^\Phi \simeq -\frac{\Phi}{re^{2\phi}\sqrt{a}}. \quad (7.17)$$

With these results we can apply consistent boundary conditions for the scalar field system. In practice, we integrate the evolution equations for Φ and Ψ all the way to the boundary (using one-sided derivatives as required). We then we can calculate the incoming eigenfield at the boundary using equation (7.17) above, and solve for the value of Π at the boundary from the eigenfield definition (7.15).

2. Numerical simulations

To specify initial data in this case we must first solve the constraint equations. A simple choice that satisfies the momentum constraint (2.22) is to assume that we start at a moment of time symmetry, which implies that both the extrinsic curvature K_{ij} and the time derivative of the scalar field Π vanish initially. We are then left with the Hamiltonian constraint (2.21), which can be further simplified by choosing the conformal metric to be initially flat. The Hamiltonian constraint then reduces to a one-dimensional Poisson-type equation for the conformal factor $\psi \equiv e^\phi$:

$$\partial_r^2 \psi + \frac{2}{r} \partial_r \psi + 2\pi \psi^5 \rho = 0. \quad (7.18)$$

For a massless scalar field the last equation becomes in fact linear in ψ , since under these assumptions $\rho = \Psi^2/\psi^4$. We are now free to specify the initial profile of the scalar field, which we choose to be a Gaussian distribution centered on the origin:

$$\Phi = \Phi_0 e^{-(r/\sigma_0)^2}. \quad (7.19)$$

We then solve the above equation for the conformal factor assuming that asymptotically it behaves as $\psi = 1 + c/r$, with c some constant.

For all the simulations presented below the parameters chosen for the initial scalar pulse are $\Phi_0 = 0.2$ and $\sigma_0 = 5.0$. Since the dynamics are now provided by the presence of the scalar field, we will also choose the lapse function to be initially unity, $\alpha(t=0) = 1$. As before, we set up our numerical grid with boundaries located at $r = 25$ and use the same grid parameters as in the previous example. In this case, for improved stability we add dissipative terms (Kreiss-Oliger dissipation) when evaluating the right hand side of equations (7.12), (7.13), and (7.14).

The evolution is somewhat similar to the case of pure gauge dynamics, the main difference being that it now represents the physical propagation of matter fields. Figure 7 shows the evolution of the scalar field in the case when we use boundary conditions based on the radial derivative method. The first panel shows the initial scalar field gaussian profile. Panels 2 and 3 show the situation at $t = 15$ and $t = 30$, when the outgoing scalar field pulse is reaching the boundary. The last panel corresponds to $t = 45$, after the pulse has gone through the boundary. Notice that the vertical scale has been changed in the last panel in order to show the small reflections introduced by the numerical boundaries, whose value is at least two orders of magnitude smaller than the size of the outgoing pulse as it reached the boundary. We also show on Figure 8 the value of the lapse function at the origin as a function of time. As can be clearly seen, the central value of the lapse initially goes down as a consequence of the curvature produced by the high matter density and reaches a minimum value of 0.5, but the configuration disperses before a trapped surface can form and the

lapse function at the origin returns rapidly to values close to 1 (this is in fact quite strong initial data, just slightly short of collapsing to a black hole). Notice that the outgoing scalar field pulse reaches the boundary at $t \sim 25$, and the small reflected pulse implodes through the origin at $t \sim 50$. The effect of these small reflections can barely be seen in the behavior of the central value of the lapse.

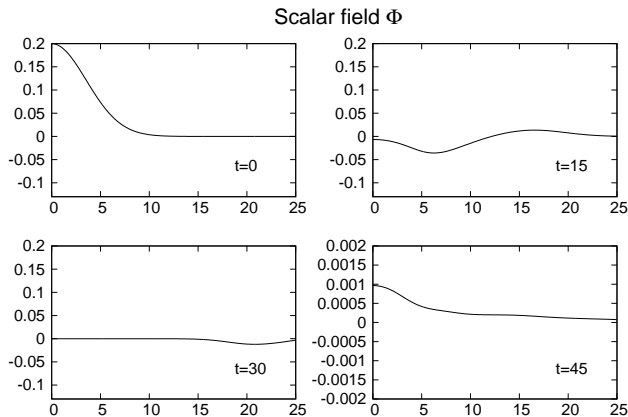


FIG. 7: Evolution of the scalar field Φ . When the pulse reaches the boundary there is a small reflection, only noticeable by rescaling the vertical range on the last panel.

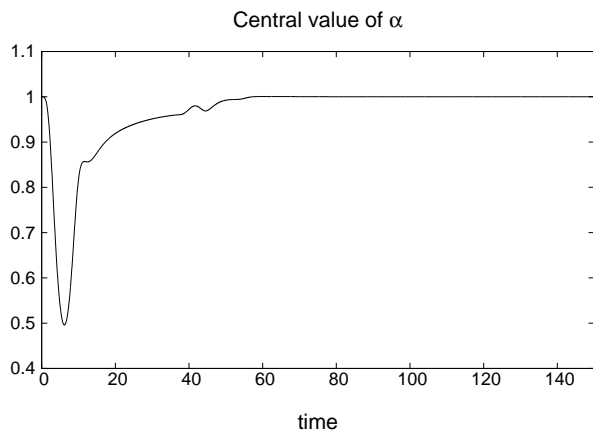


FIG. 8: Central value of the lapse function as a function of time. Initially the value of the lapse goes down as a consequence of the high curvature in the central region, but as the scalar field disperses it returns to its original value.

To further study the behavior of the reflections at the boundaries we show in Figures 9 and 10 snapshots of the evolution of the Hamiltonian and momentum constraints respectively at times $t = 23, 35, 75$, for the three different resolutions considered. As before, the values obtained for each resolution are rescaled by the appropriate factors to show fourth order convergence. Notice that in all three panels of both figures the radial axis starts at $r = 10$ in order to better appreciate the regions closest to

the boundary. The first panel in both figures shows the situation at $t = 23$, corresponding to a time just before the first pulse reaches the boundary. We can see good fourth order convergence with the exception of the two or three points closest to the boundary which appear to be converging to third order. The last two panels show the situation at $t = 35$ when the pulses have reflected from the boundary, and at $t = 75$ when the reflected pulses have imploded through the origin.

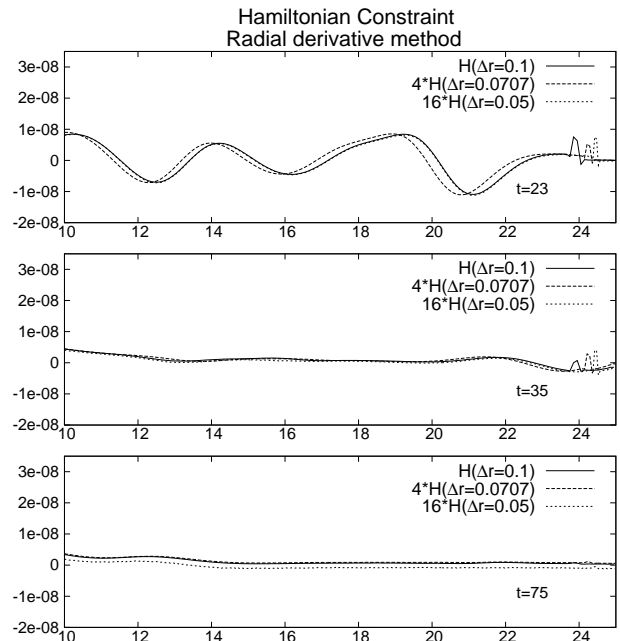


FIG. 9: Evolution of the Hamiltonian constraint using the radial derivative method. Notice that the radial scale starts at $r = 10$.

Next, in Figures 11 and 12 we consider the same simulations but now using the boundary conditions based on the time derivative method. The panels correspond to the same times as before, and the same rescaling has been used. Again we find good fourth order convergence at all times. In particular, the reflections in the momentum constraint seem smaller than those for the previous case.

The previous examples show that the constraint preserving boundary conditions work well even when matter fields are present. Although both schemes work very well in practice, we have found that the time derivative method shows cleaner convergence, so it may be preferred over the radial derivative method.

VIII. CONCLUSIONS

The aim of this paper was to present boundary conditions that are derived naturally from the hyperbolic structure of the BSSN evolution system when restricted

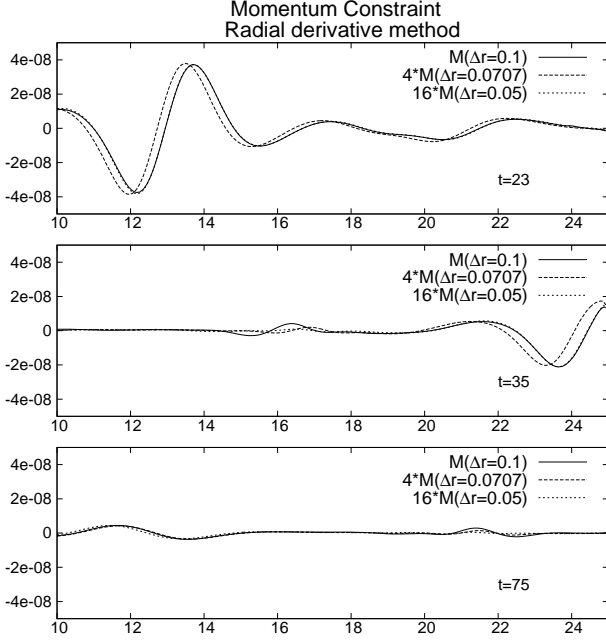


FIG. 10: Evolution of the momentum constraint using the radial derivative method. Notice that the radial scale starts at $r = 10$.

to the case of spherical symmetry. The resulting set of boundary conditions is constraint preserving in the sense that no spurious constraints violations are introduced at the boundary. Even though we do observe that the constraint residuals are reflected at the boundaries, such reflections converge to zero with increasing resolution.

The main idea of our method is to first identify the eigenfields of the evolution system, whose evolution is dictated up to principal part by simple advection equations. One can then consider separately the outgoing, incoming and non-propagating fields at the boundary. The non-propagating and outgoing fields can be evolved all the way to the boundary using one-sided derivatives when necessary. The case of the incoming fields is more subtle since the naive approach of setting them equal to zero is only consistent for plane waves in Cartesian coordinates. For most applications we may assume that the physical system studied is isolated, so that the different dynamical fields behave asymptotically as outgoing spherical waves. This assumption implies certain conditions for a subset of the incoming fields that can be used to reconstruct those fields at the boundary.

On the other hand, there exists a special type of incoming fields that need to be considered separately: those whose radial and time derivatives at the boundary can be written up to principal part as a combination of the constraints. For these fields one is not free to impose any boundary conditions, since the fact that the constraints should vanish fixes completely their evolution. In order to find those fields at the boundary one first imposes

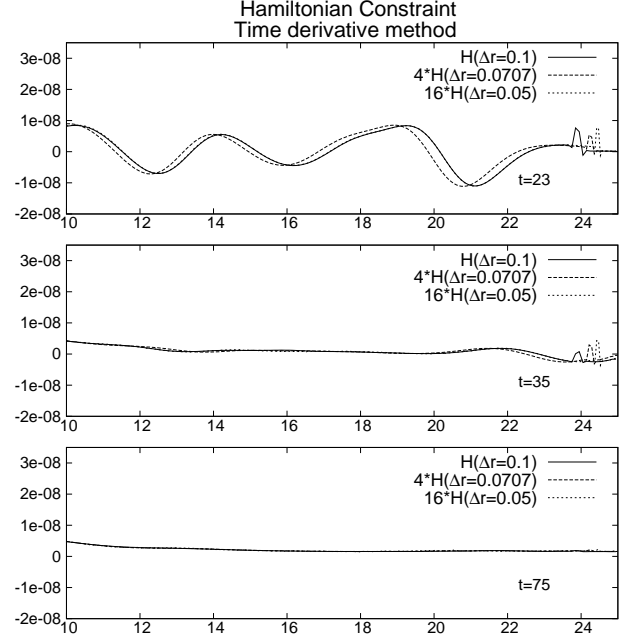


FIG. 11: Evolution of the Hamiltonian constraint. Time derivative method.

the condition that the incoming constraint combination should vanish. One can then follow two different routes: either we reconstruct the incoming fields from their radial derivative at the boundary, or we integrate them forward in time using the fact that when the constraints vanish they evolve only through source terms.

In order to show how these boundary conditions work in practice we have presented a series of numerical simulations done with our BSSN code in spherical symmetry, both for a vacuum spacetime with non-trivial gauge dynamics, and a non-vacuum spacetime with a real scalar field as the source of the gravitational field. We have shown that in both cases the two approaches used to impose constraint preserving boundary conditions work very well in practice, with the constraints converging to zero throughout the computational domain even at late times, well after the initial pulses have reached the boundaries. When comparing both approaches we find that the time derivative method shows somewhat better convergence properties than the space derivative method, particularly in the non-vacuum case.

As we mentioned previously, this approach to obtain boundary conditions arises naturally from the hyperbolic structure of the evolution system and may be generalized to the case of systems including general matter fields coupled to gravity, and with less restricting symmetry assumptions. However one must be cautious since when considering cases whose domain has two or more effective spatial dimensions there are more propagating eigenfields to be considered, and also transverse derivatives of the eigenfields appear on the analysis that need to be

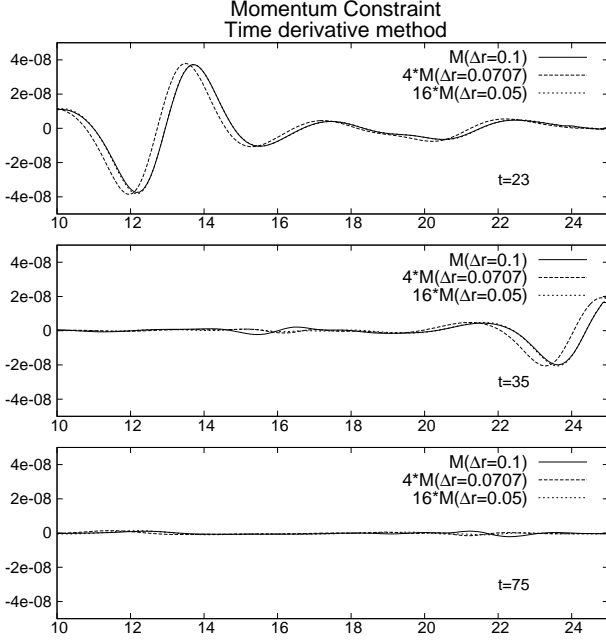


FIG. 12: Evolution of the momentum constraint. Time derivative method.

accounted for in a consistent way. Also, in this work we have taken the shift vector to be an a priori known function of space-time, but many state of the art simulations employ a dynamical shift of the Gamma-driver family [35]. The case of a Gamma-driver shift is conceptually similar to what we have discussed here, but some important subtleties arise and we prefer to leave that discussion for a further work. Finally, even in the case of axial symmetry, radiation (gravitational and otherwise) can not be assumed to vanish so that for realistic scenarios one would need to model the boundaries in a way that doesn't introduce spurious radiation into the numerical domain (this is in fact a problem that has been studied in many of the references given in the introduction, but all the details have not yet been fully addressed [36]).

Acknowledgments

This work was supported in part by CONACyT through grant 82787, by DGAPA-UNAM through grants IN113907, IN115310 and DGAPA-PAPIIT IN103514. J. M. T. also acknowledges a CONACyT postgraduate

scholarship.

Appendix A: The constraint subsystem

Here we present an analysis of the characteristic structure of the constraint subsystem. This analysis is based on that of Ref. [37], with some modifications in order to adapt it to our specific case. The constraints of the BSSN system satisfy by themselves a homogeneous subsystem of evolution equations that inherits its hyperbolicity properties from the full system. When taking into account the extra constraint C_Δ , and writing the Ricci scalar that appears in the Hamiltonian constraint in terms of the auxiliary variable Δ^r , the constraint subsystem of evolution in spherical symmetry reduces, up to principal part, to:

$$\partial_0 H \simeq 0, \quad (A1)$$

$$\partial_0 M \simeq \frac{\alpha}{6} \partial_r H + \frac{\alpha}{2a} e^{-4\phi} \partial_r^2 C_\Delta, \quad (A2)$$

$$\partial_0 (\partial_r C_\Delta) \simeq 2\alpha \partial_r M. \quad (A3)$$

One notices immediately that the Hamiltonian constraint behaves as a non-propagating eigenfield $\Omega_0 = H$, while the two combinations

$$\Omega_\pm = \frac{ae^{4\phi}H}{6} + \frac{\partial_r C_\Delta}{2} \mp \sqrt{a}e^{2\phi}M, \quad (A4)$$

propagate with eigenspeeds given by

$$\lambda_\pm^\Omega = -\beta^r \pm ae^{-2\phi} \sqrt{1/a}, \quad (A5)$$

which again are nothing more than the coordinate speed of light.

An important result regarding the constraint eigenfields Ω is that each one is related to an eigenfield ω of the full evolution system that propagates with the same speed, satisfying

$$\Omega \simeq s^i \partial_i \omega,$$

with \vec{s} a vector that characterizes the propagation direction. For our case it turns out that $\lambda_\pm^\Omega = \lambda_\pm^\omega$ and thus

$$\Omega_\pm \simeq \partial_r \omega_\pm^l, \quad (A6)$$

which is the relation we use in order to construct constraint adapted boundary conditions.

-
- [1] J. York, in *Sources of Gravitational Radiation*, edited by L. Smarr (Cambridge University Press, Cambridge, England, 1979).
 - [2] T. W. Baumgarte and S. L. Shapiro, *Phys.Rev.* **D59**, 024007 (1998).

- [3] M. Shibata and T. Nakamura, *Phys.Rev.* **D52**, 5428 (1995).
- [4] H. Friedrich, *Proc. Roy. Soc. London* **A378**, 401 (1981).
- [5] H. Friedrich, *Comm. Math. Phys.* **100**, 525 (1985).
- [6] H. Friedrich, *Class. Quantum Grav.* **13**, 1451 (1996).

- [7] H. Friedrich and A. D. Rendall, Lect. Notes Phys. **540**, 127 (2000).
- [8] D. Hilditch, Int.J.Mod.Phys. **A28**, 1340015 (2013).
- [9] H. Friedrich and G. Nagy, Comm. Math. Phys. **201**, 619 (1999).
- [10] B. Szilágyi, R. Gómez, N. T. Bishop, and J. Winicour, Phys. Rev. **D62**, 104006 (2000).
- [11] B. Szilagyai and J. Winicour, Phys. Rev. **D68**, 041501 (2003).
- [12] G. Calabrese and O. Sarbach, J. Math. Phys. **44**, 3888 (2003).
- [13] O. Reula and O. Sarbach, J. Hyperbol. Diff. Equat. **2**, 397 (2005).
- [14] O. Sarbach and M. Tiglio, J. Hyperbol. Diff. Equat. **2**, 839 (2005).
- [15] H. Beyer and O. Sarbach, (2004).
- [16] G. Nagy and O. Sarbach, Class. Quant. Grav. **23**, S477 (2006).
- [17] M. C. Babiuc, B. Szilagyai, and J. Winicour, Phys. Rev. **D73**, 064017 (2006).
- [18] O. Sarbach and M. Tiglio, Living Rev.Rel. **15**, 9 (2012).
- [19] J. Winicour, Class.Quant.Grav. **29**, 113001 (2012).
- [20] C. Bona and C. Bona-Casas, Phys.Rev. **D82**, 064008 (2010).
- [21] D. Hilditch *et al.*, Phys.Rev. **D88**, 084057 (2013).
- [22] D. Nunez and O. Sarbach, Phys.Rev. **D81**, 044011 (2010).
- [23] G. Calabrese, L. Lehner, and M. Tiglio, Phys. Rev. **D65**, 104031 (2002).
- [24] G. Calabrese *et al.*, Commun. Math. Phys. **240**, 377 (2003).
- [25] M. C. Babiuc, H. O. Kreiss, and J. Winicour, Phys. Rev. **D75**, 044002 (2007).
- [26] H. O. Kreiss and J. Winicour, Class. Quant. Grav. **23**, S405 (2006).
- [27] L. T. Buchman and O. C. A. Sarbach, Class. Quant. Grav. **23**, 6709 (2006).
- [28] H. O. Kreiss, O. Reula, O. Sarbach, and J. Winicour, Class. Quant. Grav. (2007), to appear.
- [29] L. T. Buchman and O. C. A. Sarbach, Class. Quant. Grav. **24**, S307 (2007).
- [30] J. D. Brown, Phys.Rev. **D79**, 104029 (2009).
- [31] M. Alcubierre and M. D. Mendez, Gen.Rel.Grav. **43**, 2769 (2011).
- [32] M. Alcubierre, *Introduction to 3+1 Numerical Relativity* (Oxford Univ. Press, New York, 2008).
- [33] C. Bona, J. Massó, E. Seidel, and J. Stela, Phys.Rev.Lett. **75**, 600 (1995).
- [34] M. W. Choptuik, Phys. Rev. Lett. **70**, 9 (1993).
- [35] M. Alcubierre *et al.*, Phys. Rev. **D67**, 084023 (2003).
- [36] H. Friedrich, Gen.Rel.Grav. **41**, 1947 (2009).
- [37] C. Gundlach and J. M. Martín-García, Phys. Rev. **D70**, 044032 (2004).